Anomalously deep polarization in SrTiO₃ (001) interfaced with an epitaxial ultrathin manganite film

Zhen Wang,[1,2] Jing Tao,[2] Liping Yu,[3] Hangwen Guo,[1] Lina Chen,[1] Myung-Geun Han,[2] Lijun Wu,[2] Huolin Xin,[2]
Kim Kisslinger,[2] E. W. Plummer,[1,*] Jiandi Zhang,[1,†] and Yimei Zhu[2,‡]

[1]*Department of Physics & Astronomy, Louisiana State University, Baton Rouge, Louisiana 70803, USA*
[2]*Department of Energy Science and Technology, Brookhaven National Laboratory, Upton, New York 11973, USA*
[3]*Department of Physics, Temple University, Philadelphia, Pennsylvania 19122, USA*

Using atomically resolved imaging and spectroscopy, we reveal a remarkably deep polarization in nonferroelectric SrTiO₃ near its interface with an ultrathin nonmetallic film of La$_{2/3}$Sr$_{1/3}$MnO₃. Electron holography shows an electric field near the interface in SrTiO₃, yielding a surprising spontaneous polarization density of $\sim$21 μC/cm^2. Combining the experimental results with first-principles calculations, we propose that the observed deep polarization is induced by the electric field originating from oxygen vacancies that extend beyond a dozen unit cells from the interface, thus providing important evidence of the role of defects in the emergent interface properties of transition metal oxides.

I. INTRODUCTION

The last couple of decades witnessed the discovery of extraordinary phenomena at the interface of transition metal oxides (TMOs), which are related, but not identical to, the bulk properties [1–4]. Electronic reconstruction [5], such as charge transfer [6], has been regarded as an important driving force. In many cases, structural relaxation, reconstruction, or distortions [7] can profoundly impact the properties at interface. Microscopic characterization of lattice structure and chemical composition is an essential step towards understanding the nature of interface properties. Here, we report upon a remarkably deep polarization of the nonferroelectric SrTiO₃ (STO) near its interface with an ultrathin nonmetallic film of La$_{2/3}$Sr$_{1/3}$MnO₃ (LSMO) discovered using atomically resolved scanning transmission electron microscopy (STEM) imaging and electron energy-loss spectroscopy (EELS). We demonstrate that by combining the experimental results with first-principles calculations, the observed deep polarization is induced by the electric field originating from oxygen vacancies.

The STO is an archetypal substrate material because of its compatible cubic perovskite structure. Novel properties appear at the interface of STO with other transition-metal compounds. Two-dimensional electron gas [8], and even superconductivity [9], appear at the interface between STO and LaAlO₃ (LAO). Compared with its bulk, giant enhancement of superconductivity was revealed at the interface of STO with a single layer of FeSe [10]. A metallic surface state exists on STO (001) [11] and may be related to the presence of oxygen vacancies [12]. These observations suggest that the interface is more complex than anticipated, including possible charge transfer [6], lattice relaxation [7], stoichiometric variation [13,14], defect effect [15–18], and thickness-dependent interfacial coupling [19].

To date, most studies focused on the properties of interfaces and deposited films, while the changes of substrate bulk received little attention, even though changes in the substrate may play a critical role in the new phenomena of the heterostructures. Undoped bulk STO is a nonferroelectric material at room temperature. A small lattice distortion in STO was observed up to 6 unit cells (u.c.) from the interface, induced by oxide overlayers such as LAO [20–22]. Pure STO is an incipient ferroelectric, though it is a paraelectric at low temperature due to antiferrodistortion and quantum fluctuations [23,24]. The breaking of symmetry triggered by the electric field activates the ferroelectric TO phonon mode and induces local ferroelectric order [25]. In the presence of a dopant, such as Ca, Bi, or O, bulk STO displays ferroelectric properties at low temperatures [26–28]. The STO films under strain reportedly are ferroelectric at room temperature [29]. However, there has been no observation of large polarization in STO at room temperature without doping or strain.

II. EXPERIMENTS

The LSMO film was grown on TiO₂-terminated STO (001) substrate by ultrahigh vacuum pulsed-laser deposition method. The LSMO was deposited at 700 °C. Oxygen pressure was set at 80 mTorr with 6% of ozone. After deposition, the sample was cooled at a rate of 15 °C/min in a 100 mTorr 6% ozone environment. Our *in situ* low-energy electron diffraction (LEED) images confirmed that the epitaxial LSMO film follows the in-plane symmetry of the substrate without surface reconstruction.

Cross-sectional TEM samples were cut into 80-nm-thickness by a focused ion beam (FIB) with Ga$^+$ ions and were further milled using Nanomill with Ar$^+$ ions to remove the surface damage on the samples. All the samples were studied using the 200 kV JEOL ARM electron microscope at Brookhaven National Laboratory (BNL) equipped with two aberration correctors, a dual-energy-loss spectrometer and a cold field emission source. The atomic structures of the samples were studied in atomic-resolution high-angle annular dark-field (HAADF) and annular bright-field (ABF) STEM imaging modes. The STEM imaging conditions were optimized for the EELS spectroscopic with a probe size of 0.8 Å, a convergence semi-angle of 20 mrad, and the collection semi-angle of 88 mrad. Line-scanning EELS spectra were obtained across the interface with a step size of 0.12 Å and a dwell time of 0.05 s/pixel. To correct the intrinsic shift

*wplummer@phys.lsu.edu
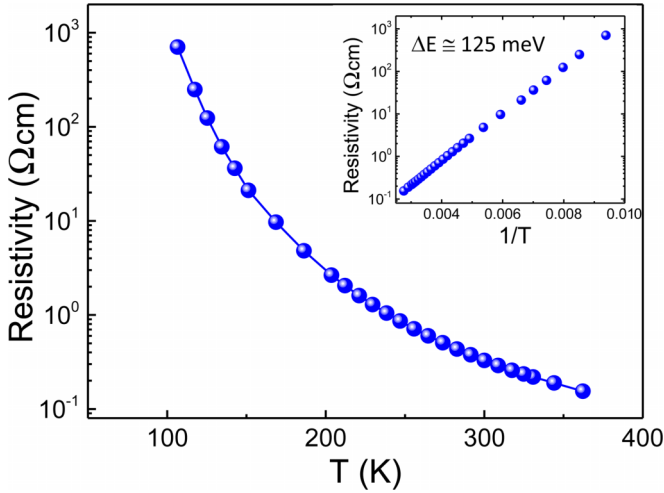†jiandiz@lsu.edu
‡zhu@bnl.gov

FIG. 1. Temperature dependence of resistivity for 4 u.c. LSMO/STO heterostructure. Inset is the resistivity versus the $1/T$ profiles with the activation energy (ΔE).

of energy of the electron beam, the zero-loss peak was collected simultaneously with the core-loss spectra in the EELS line-scanning process. The EELS spectra were background subtracted with a power-law function, and multiple scattering was corrected by a Fourier deconvolution method. A dispersion of 1 eV/channel was selected to simultaneously collect the Ti-L, O-K, Mn-L, La-M, and Sr-L edges for composition distribution investigation. To study the fine structure of the Ti-L, O-K, and Mn-L edges, a dispersion of 0.1 eV/channel was used with an energy resolution of ~0.5 eV. Electron holography experiments were carried out using a dedicated Lorentz microscope at BNL.

III. RESULTS AND DISCUSSION

The LSMO/STO heterostructure is not metallic when the thickness of LSMO film is less than 6 u.c. [30]. The insulating behavior of the 4 u.c. LSMO film is confirmed by temperature dependent resistivity measurements of our samples, as displayed in Fig. 1. The epitaxial LSMO film follows the in-plane symmetry of the substrate (as illustrated at the top right of Fig. 2). The lattice mismatch between bulk LSMO and bulk STO is less than 1%. Figure 2(a) is a HAADF-STEM image obtained from the 4 u.c. LSMO film on STO viewed along [100] direction, indicating an atomically sharp interface. The contrast of the HAADF-STEM image can be directly related to the atomic number (Z), i.e., the heavier the atom, the brighter the atomic column appears in the image. The inset in the top right corner is an enlarged section of the image, showing the stacking atomic planes across the interface. As marked by the dashed line, the STO substrate terminates with a TiO$_2$ layer, and the LSMO film starts to grow with a (La/Sr)O layer.

Surprisingly, the HAADF-STEM image in Fig. 2(a) reveals a pronounced atomic displacement of Ti sites in the STO towards the interface and Mn sites as well towards the surface of the LSMO film. This Ti displacement can clearly be seen in the magnified u.c. in the boxed areas marked with white squares. The atomic displacements of Ti (δ_{Ti}: distance from
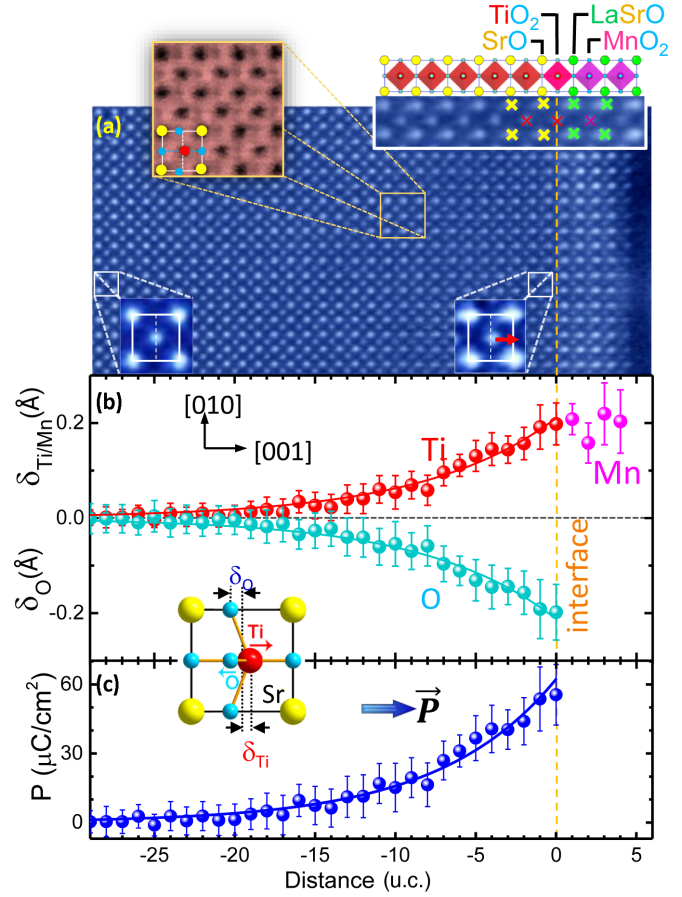

FIG. 2. (a) A HAADF-STEM image of the interface region of 4 u.c. LSMO film on STO(001) along the [100] direction. The top right corner is an enlarged image with schematic structure with the TiO$_2$ termination of STO. A zoom-in ABF-STEM (upper left) and two HAADF-STEM images from the marked area show distinct shifts of the Ti- and O- atoms resulting a buckling in TiO$_2$ layer. (b) Measured B site (Ti, Mn) and O displacements as a function of position across the interface ($x = 0$) with a schematic STO unit cell in the inset and the exponential fitting profile (solid curves). The δ_O values close to the interface were not directly measured due to the relatively weak oxygen signals in the ABF image. (c) The polarization density p of STO derived from the atomic displacements in (b) and the fitting profile.

Ti to the centrosymmetric center of the cubic u.c.) measured from the HAADF-STEM images are plotted (red dots) in Fig. 2(b) as a function of the distance from the interface, with the measurements averaged over 20 u.c. along the b axis. There is an unexpectedly large Ti-displacement in the vicinity of the interface with respect to the La/Sr positions. To rule out possible nonintrinsic displacement in measurements, we undertook a thorough quantitative analysis. The analysis suggests imaging conditions and small local sample curling could engender a Ti displacement in atomic images, and great care must be to be taken to remove possible artifacts. By carefully determining the sample curling geometry, using bi-Gaussian fitting of experimental images with asymmetric atom intensities, and deconvoluting sample-curling effect, we conclude that the atomic displacement observed near the interface in Fig. 2 is both intrinsic and reproducible (see the Appendix).
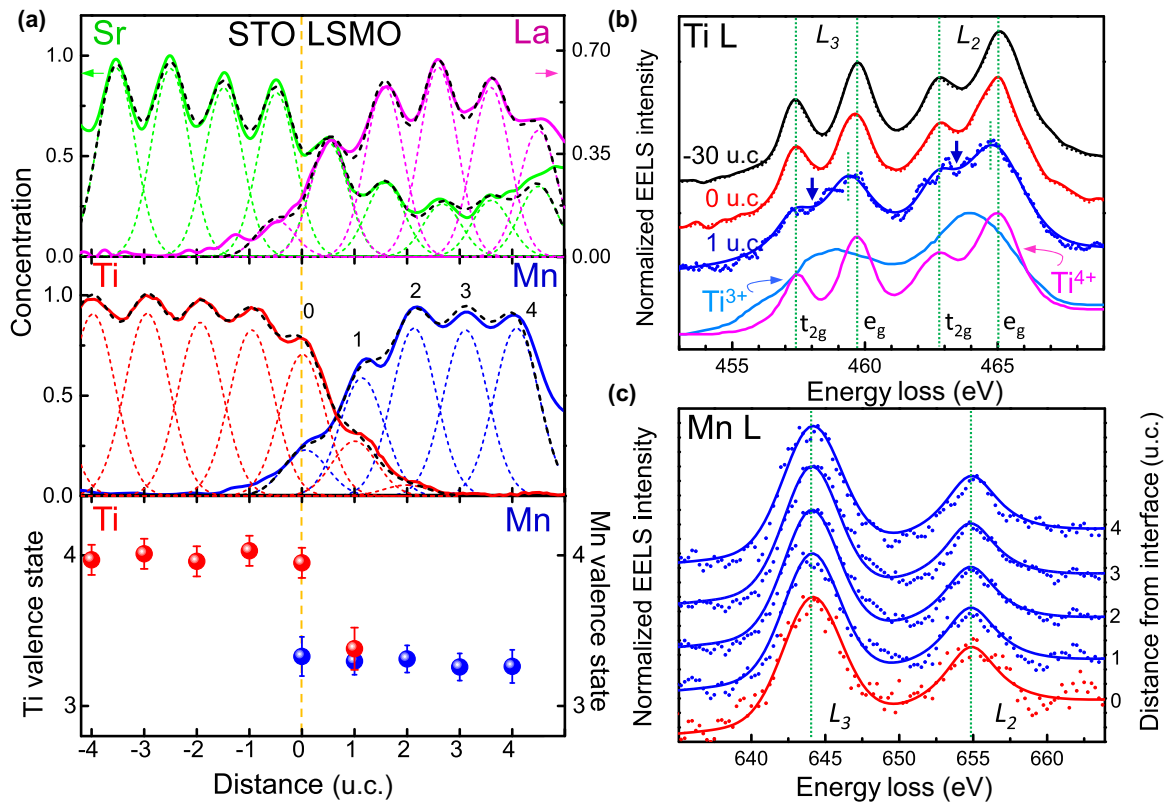
FIG. 3. (a) Chemical composition profiles extracted from the (top) (La-M,Sr-L) edges and (middle) (Ti, Mn)-L edges, showing chemical intermixing at the interface, and (bottom) Ti and Mn oxidization states. La and Sr concentration is normalized to the stoichiometry composition 0.67 in LSMO and 1 in STO, respectively. (b) Ti-$L_{2,3}$ edges extracted from the position 30 u.c. away from the interface (black), the TiO$_2$ termination layer (red), Ti in the first MnO$_2$ layer (blue) (the dots are the raw data and the lines represent the fitted results), and the reference spectra of Ti^{3+} (light blue) and the Ti^{4+} (red), respectively. The peak intensities are normalized with e_g peaks of the L_2 edges. (c) Mn $L_{2,3}$ edges obtained from the LSMO film (blue) to Mn in the TiO$_2$ termination layer (red), normalized with the Mn L_3 edge.

We further used ABF-STEM imaging, sensitive to light elements, to locate the position of oxygen in a unit cell. An ABF-STEM image obtained from the area marked with the yellow square is shown at the top left corner of Fig. 2(a). This ABF-STEM image reveals that the O ions in the TiO$_2$ planes are also displaced from the centrosymmetric center, where, in both cases (Ti and O), the A(Sr) site is used as a reference for the measurement. The atomic displacements of oxygen in the TiO$_2$ planes (δ_O, in contrast to Ti, the opposite shift of O from the centrosymmetric center of the cubic u.c.) are plotted (green dots) in Fig. 2(b), obtained by assuming a constant $\delta_O : \delta_{Ti} \sim 1.0$ throughout the STO substrate [31,32]. The value of the δ_O:δ_{Ti} ratio was determined through averaging all the data points. The magnitude of δ_o and δ_{Ti} decreases as a function of distance from the interface and becomes undetectable beyond the 20th u.c.

Given the displacement measurements of the positive-charge center (δ_{Ti}) and negative-charge center (δ_O) from the centrosymmetric center of the undistorted cubic perovskite structure [depicted in the model in the inset of Fig. 2(b)], we calculated the polarization density (p) of the STO substrate and plotted it in Fig. 2(c) (using the Ti^{4+} valence state) by using $p = \frac{\sum_i Z_i \delta_i}{V_{uc}}$, where Z_i is the Born effective charge [33] of each atom in a unit cell, δ_i (i denotes either Ti or O) is the distance off the centrosymmetric center, and V_{uc} is the unit cell volume of cubic STO. The

polarization was found to be about 54 μC/cm^2, 1 u.c. from the STO/LSMO interface, and the averaged value over the 20 u.c. in STO is about 21 ± 10 μC/cm^2. This is a very large polarization density for an undoped STO bulk material at room temperature compared to the previously reported values [34].

Figure 3(a) displays the elemental distribution crossing the STO/LSMO interface, including Ti, Mn, La, and Sr, all quantified from the intensities of core-loss spectra obtained with atomically resolved EELS. All the intensities are normalized with bulk STO (for Sr and Ti), and for thick LSMO films (for La and Mn). The local profiles of elemental concentration were extracted by fitting a series of Gaussian peaks, fixed at each of the atomic columns [35]. There is a 1 u.c. intermixing of Mn and Ti at the STO/LSMO interface: $\sim(23 \pm 5)$% of Ti diffuses into the first MnO$_2$ layer in the LSMO film, and (20 ± 5)% of Mn from the LSMO film mixes into the TiO$_2$ termination layer of the STO substrate. It is also apparent that the concentration of La in the first La/SrO layer of the LSMO film is only about 60% of that inside the film. Meanwhile, less than (10 ± 5)% La diffused into STO up to two atomic layers from the interface, thus implying a large off-stoichiometry of Sr at the interface. In the LSMO film, Sr segregation occurs both near the interface and the surface, indicating layer-by-layer dependence of the Sr concentration in the LSMO film [36].

We characterized the valence charges of Ti and Mn by EELS to gain insight into the phenomenon of polarization.
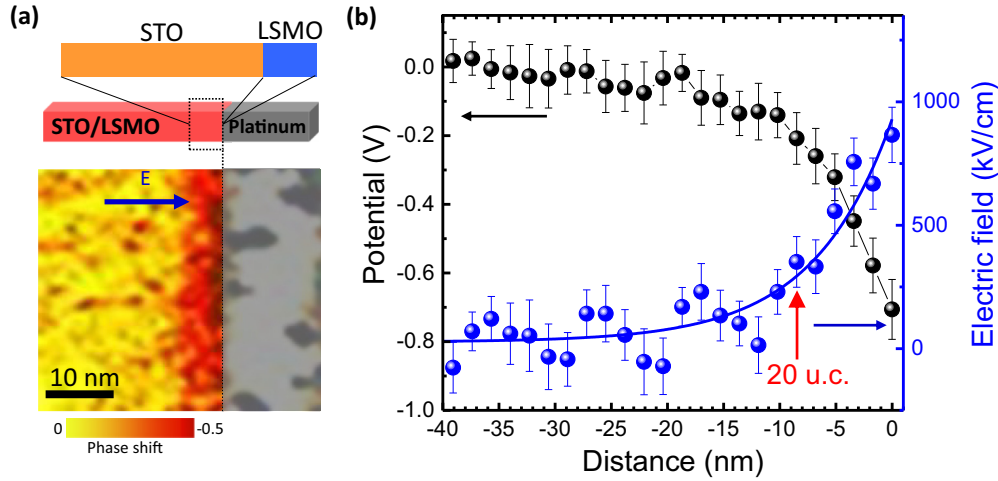
FIG. 4. (a) (top) Schematic of the corresponding region and (bottom) reconstructed electron holographic phase image of the LSMO/STO heterostructure. (b) Electric potential and filed profiles in STO calculated from the phase image.

The bottom of Fig. 3(a) plots the valences of both Ti and Mn versus their position through probing the Ti-L edge and the Mn-L edge. Figure 3(b) shows the Ti $L_{2,3}$ edge at 30 u.c. distance from the interface (black), the TiO_2 termination plane (red), and the Ti-doped MnO_2 layer (blue). The bottom two curves in Fig. 3(b) are the Ti-L edge of reference spectra for a formal valence of Ti^{4+} and Ti^{3+} [37]. The Ti $L_{2,3}$ edge spectrum (blue) in the first MnO_2 layer differs from those from both the Ti^{4+} and Ti^{3+} formal valence states. It indicates that substitutional Ti in the LSMO film has a reduced Ti valence state compared with 4+ in STO. Fitting the measured spectra of the Ti-L edge gives a valence about 3.4+ for Ti in the LSMO film. Also, a small variation of the O-K edge fine structure was observed in the STO polarized region, in agreement with the trends reported as a result of oxygen vacancies in STO [37]. Even though the changes are small, they highlight the existence of oxygen vacancies, which donate electrons to the interface, as we will discuss later. Figure 3(c) shows the Mn-L edge for the Mn in the top STO layer (red) and in the LSMO film (blue). By measuring the $L_{2,3}$ ratio [38], we estimated that the valence state of the Mn ions is around 3.3+. This means that substitutional Mn in the STO substrate does not change its valence state, in contrast to substitutional Ti in LSMO film. In our sample, we did not observe a reduced valence state of Mn at the interface, as reported in YBCO/LCMO and STO/LSMO film [39,40], which might be caused by the combination of Sr segregation/defects and polar potential at the interface and surface in our ultrathin film.

To confirm our derived polarization, we undertook off-axis electron holography on the LSMO/STO interface and observed an electric-field gradient in the STO pointing toward the interface. The off-axis electron holography technique can be used to map the electrostatic potentials and the distribution of the electric field in a film [41]. The distributions of electrostatic potential were determined by the electron-wave phase retrieval, and derived from the function $V = \frac{\Delta\phi}{c_E t}$. Here, $\Delta\phi$ represents the phase shift, and t is the sample's thickness, measured from holography experiments. Also, c_E is taken as the value of 0.00729 rad V^{-1} nm^{-1} for an accelerating voltage of 200 kV. The thickness profile of the LSMO/STO sample

was also estimated from the holographically reconstructed amplitude image. The electric field was obtained by taking the first derivative of profile of the potential line. The spatial resolution of our measurements is about 1.36 nm. The accuracy of our measurements is about 0.1 V.

The bottom of Fig. 4(a) is the phase map extracted from the holographic data, with the red areas denoting the change in potential. The profiles of the electric potential and the field from a polarized region are plotted as a function of distance from the interface in Fig. 4(b). The built-in electric field points from the substrate to the interface. The averaged electric field at a distance of 7 nm is ∼654 kV/cm. Although the dielectric constant ε_{STO} of STO is known to depend on the applied electric field, there is no report on ε_{STO} under an electric field as large as a few thousand kV/cm. From the literature, it appears that ε_{STO} has little electric-field dependency at room temperature [34]. Therefore, $\varepsilon_{STO} = 300$ [42] is a fair assumption under high electric fields. Then, the averaged polarization density in STO is estimated to be $P = \varepsilon_{STO}\varepsilon_0 E_{STO} \sim 18 \pm 6 \, \mu C/cm^2$ in a volume of the bulk STO of about 6–8 nm (15–20 u.c.) from the interface. We note that this polarization density is an estimate due to the limited spatial resolution in electron holography; it is consistent with our STEM results ($21 \pm 10 \, \mu C/cm^2$) obtained from the data shown in Fig. 2(c).

The large polarization observed in STO/LSMO heterostructures with a broad extension into STO for more than 20 u.c. is astonishing. Unlike $BaTiO_3$, bulk STO is not ferroelectric. Nevertheless, it is known that the Ti cation in the TiO_6 octahedron is small and can easily be displaced from its central position [43]. In particular, near the interface, many factors may contribute to the cation-oxygen displacements observed in our experiments: (1) polar discontinuity and (2) defects. Interfacial intermixing induced Mn-on-Ti (denoted as Mn_{Ti}, i.e., replacing one Ti by Mn) defects in STO, La_{Sr} defects in STO or O vacancies (V_O) in STO, and homogeneous/inhomogeneous La/Sr ratios in LSMO.

We performed first-principles calculations to elucidate the role of these possible contributors. The first-principles calculations are based on the density functional theory (DFT) with the generalized gradient approximation (GGA) [44]. We
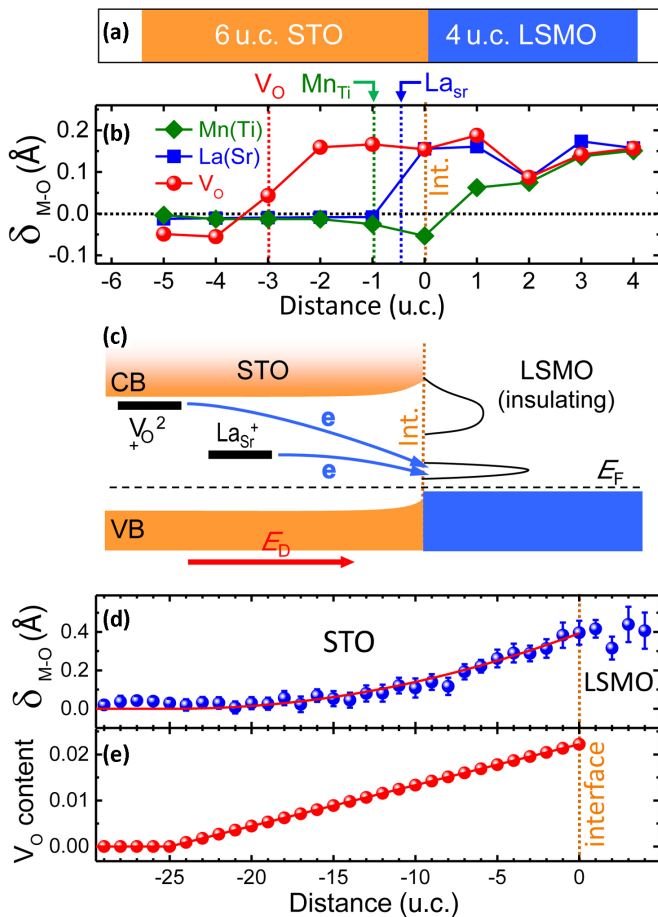
FIG. 5. (a) Schematic of the 6 u.c. STO/4 u.c. LSMO interface. (b) The $\delta_{M\text{-}O}$ displacements induced by O-vacancy (V_O), La-on-Sr (La_{Sr}), and Mn-on-Ti (Mn_{Ti}) defects, respectively. The locations of these defects are indicated by dashed vertical lines. (c) Schematic defect-level and band diagram of the STO interfaced with LSMO film. The red arrow denotes the electric field (E_D) created by the charge transfer from V_O or La_{Sr} donor defects to the empty states above the Fermi energy (E_F) of LSMO. (d) The $\delta_{M\text{-}O}$ displacements fitted with calculated one caused by V_O (red curve) with concentration shown in (e).

used the plane-wave projector-augmented wave (PAW) [45] method as implemented in the Vienna *Ab initio* Simulation Package (VASP) code [46]. The Hubbard "$+ U$" (3 eV) correction was applied to the Mn $3d$ states, following the simplified rotationally invariant "U" scheme proposed by Dudarev *et al.* [47]. The dipole correction [48] was applied in order to remove the artificial dipole interaction caused by using the supercell method for slab systems. The LSMO/STO (001) interface is modeled by a supercell containing 6 u.c. STO and 4 u.c. LSMO along z direction and 1×3 u.c. in the x-y plane. In the calculations, periodic boundary conditions were used in all directions, and a 15 Å vacuum space was inserted along the z direction. An $8 \times 3 \times 1$ or $3 \times 8 \times 1$ k-point grid was used to sample the Brillouin zone during structural relaxation. An energy cutoff of 400 eV was used. All atoms were fully relaxed until their atomic forces were less than 0.02 eV/Å.

Figure 5(a) shows the schematic supercell structure of our model system, consisting of 6 u.c. of STO and 4 u.c. of LSMO.

For the defect-free STO/LSMO interface considered, our calculations show that the resulting cation-oxygen displacements ($\delta_{M\text{-}O}, M = $ Ti,Mn) are less than 0.02 Å, which is at least one order of magnitude smaller than the experimentally measured values. The sign of $\delta_{Mn\text{-}O}$ is also opposite of the experimental ones. Hence, the observed large $\delta_{Mn\text{-}O}$ cannot be attributed as being an intrinsic property of the defect-free interfaces.

The structural relaxation of our model systems with defects, denoted as V_O, La_{Sr}, or Mn_{Ti}, was calculated separately. The calculated defect-induced cation-oxygen displacements ($\delta_{M\text{-}O}$) are shown in Fig. 5(b). The Mn_{Ti} defects result in a rather small negative $\delta_{Ti\text{-}O}$ in STO near the interface, which is similar to that in the defect-free scheme. In contrast, La_{Sr} and Vo defects induce large positive $\delta_{Ti\text{-}O}$ in the region sandwiched by the defective layer and the interface. The calculated $\delta_{Ti\text{-}O}$ values are comparable to the experimental values near the interface.

Such a defect-induced polarization scenario can be understood from the defect level and the band diagram of the STO/LSMO interface, shown in Fig. 5(c). $La_{1-x}Sr_xMnO_3$ can be viewed as the Sr-doped $LaMnO_3$ (LMO). The LMO is an insulator with an optical band gap of ~ 1.03 eV; its valence band maximum (VBM) is located ~ 1 eV below the STO conduction band minimum (CBM) when interfacing with STO [49]. The substitution of La^{3+} by Sr^{2+} ions (i.e., Sr_{La}) produces holes in the LMO valence states, and the Fermi level shifts down with increasing x [50]. When the Fermi level is lower than the donor levels of the V_O and La_{Sr} defects, which are ~ 0.2 eV and ~ 1.2 eV below STO CBM, respectively [18], the electrons will transfer from the donor defects to the empty states of LSMO above the Fermi level. Such charge transfer builds up an electric field [E_D, see Fig. 5(c)], in agreement with our electron-holography measurement (Fig. 4). The electric
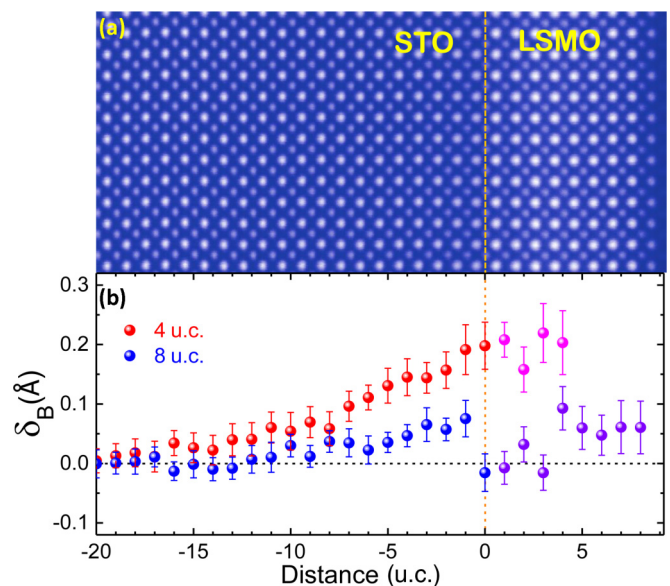

FIG. 6. (a) The HAADF-STEM images for 8 u.c. LSMO film on STO (001) viewed along the [100] direction. The yellow dotted line indicates the interface, and STO is terminated with a TiO_2 layer (where $x = 0$). (b) Measured $\delta_B (B = $ Ti and Mn) displacements as a function of distance from the interface by averaging over 30 u.c. along the interface.
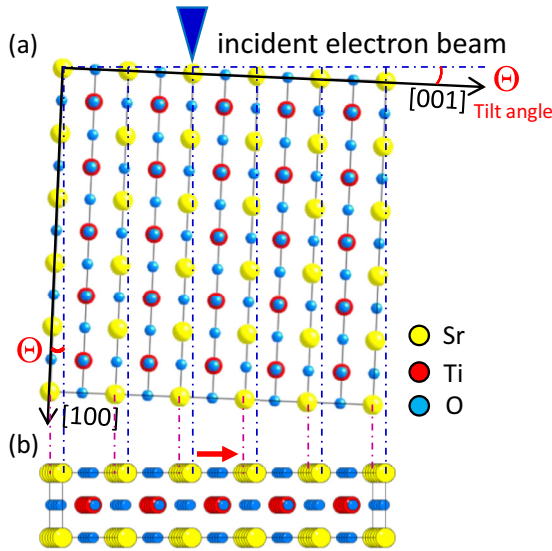
FIG. 7. (a) Schematic diagram of the [100] oriented STO crystal with a small tilt angle (Θ) towards the [001] direction. (b) The projected atomic columns along the incident-beam direction. The small local crystal tilt/curling yields elongated projected potentials, thus asymmetric image intensity of atomic columns in the direction are indicated by the red arrow.

field, E_D, then pushes Ti ions toward the interface and O ions away from the interface, respectively, leading to a positive δ_{M-O} in the STO side near the interface.

Within the above defect scheme, it is expected that the amplitude of δ_{Ti-O} depends on the defect position and concentration: the higher the concentration of V_O and La_{Sr} defects near the interface, the larger the δ_{Ti-O}. The observed δ_{Ti-O} in STO must reflect the convoluted effects of these different defects at different locations. Our experiment indicates that La_{Sr} defects are mainly confined within one u.c. in the STO from the interface, so the experimentally observed δ_{Ti-O} in deep STO most likely originates from the V_O defects. Assuming that the O vacancies are the only cause of the observed polarization in STO, and distribute in the STO near the interface, we can fit the observed δ_{Ti-O} displacements very well with the convoluted contributions of V_O from different layers, obtained from our theoretical calculations shown in Fig. 5(d). The fitted V_O distribution is shown in Fig. 5(e), decreasing linearly from ~2.2% at the interface to zero at 25 u.c. away from the interface and into the bulk of STO.

Figure 5(c) suggests that the amplitude of δ_{Ti-O} also depends on the energy difference between the V_O donor level at the STO side and the Fermi level of LSMO. The larger the energy difference, the stronger the electric field, and the deeper the polarization. Our preliminary study indicates that the δ_{Ti-O} displacements in STO interfaced with thicker metallic LSMO films are significantly reduced. As shown in Fig. 6(b), compared with the 4 u.c. LSMO/STO, the δ_{Ti} displacements in 8 u.c. LSMO/STO only extends to ~10 u.c. from the interface, with much reduced displacement values. Such a reduction may be attributed to the change of the Fermi level in LSMO. In other words, our model suggests that the interface polarization
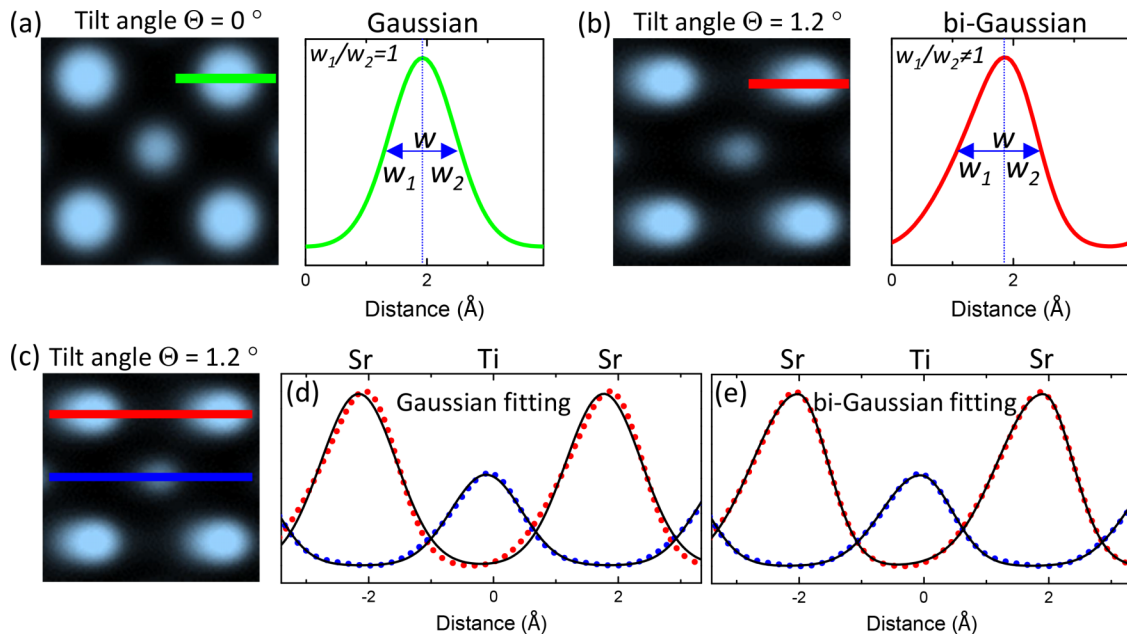

FIG. 8. The simulated HAADF-STEM images of STO with and without small crystal curling. For the STEM image without crystal curling, the atom intensity can be well fitted with a single-Gaussian function (a). In contrast, for the crystal with slight curling, they cannot be well fitted with a single Gaussian but with a bi-Gaussian function (b). The bi-Gaussian function is defined by (a) and (b). Simulated HAADF-STEM images for noncurling (a) and curling (b) STO crystal using the BNL developed computer codes are based on multislice calculations with frozen phonon approximation. Intensity profiles across the Sr column in the images are shown on the right. The parameters $w1$ and $w2$ are the full width at half maximum for the left and right side of the peak, respectively. (c), (d) Simulated HAAD-STEM image (c) and intensity profiles of Sr columns (red) and Ti columns (blue) with fitting profiles (black), using a single-Gaussian (d) and a bi-Gaussian function (e). The bi-Gaussian fitting shows better agreement with the simulated intensity profiles.

in the STO side should also be tunable by choosing different film materials that have different band offsets with STO or the work functions.

In summary, we observed an unexpectedly large interface-induced polarization in dielectric $SrTiO_3$ in the vicinity of a nonmetallic LSMO film. We demonstrate that this spontaneous polarization is caused by an intrinsic electric field arising from the STO/LSMO heterostructures and that this electric field is induced by a built-in interfacial potential originating from the chemical defects. These intriguing effects in perovskite STO may inspire researchers to further pursue studies of emergent properties by nanoscopically probing the effects from lattice distortion and compositional variation in epitaxial oxide heterostructures.

APPENDIX: THE EFFECTS OF SAMPLE TILT/CURLING ON THE MEASUREMENT OF POLARIZATION-INDUCED ATOMIC DISPLACEMENT

1. The effect of slight sample-curling on HAADF-STEM images

In atomic imaging of transmission electron microscopy or STEM, small curling at the very thin edge of the sample is largely unavoidable. Very often, the atom positions we observe are convoluted with the curling-induced local crystal tilt. Figure 7 illustrates the geometry of a [100]-oriented STO crystal, curling towards the [001] direction. The crystal model in Fig. 7 was used in our HAADF-STEM image simulation to correct possible artifacts due to the sample curling. The very slight tilt results in asymmetric intensity distribution of atomic columns, which deviates from the symmetric Gaussian function commonly used to do atomic column fitting in the STEM images.

2. Extracting atomic positions by using Gaussian and bi-Gaussian fitting methods

$$y = y_0 + He^{-0.5\left(\frac{x-xc}{w1}\right)^2} \ (x < x_c)$$

$$y = y_0 + He^{-0.5\left(\frac{x-xc}{w2}\right)^2} \ (x \geqslant x_c),$$
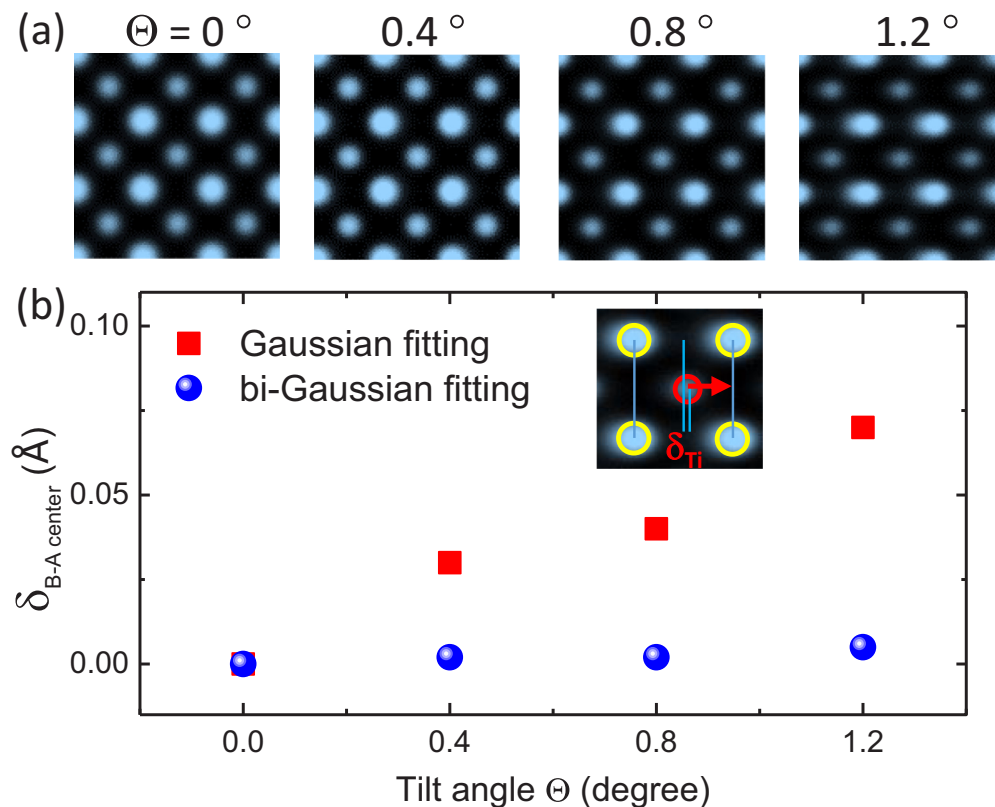

FIG. 9. (a) Simulated HAADF-STEM images of STO crystal along the [100] direction, with different tilt angles. (b) The relative *B* site (Ti ions) displacements with respect to *A* site (Sr ions) center, $\delta_{B\text{-}A\ \text{center}}$, as a function of sample tilt angles, were measured by Gaussian (red) and bi-Gaussian fitting (blue) methods. The inset in (b) shows the direction of polar displacement towards sample curling direction, as marked by the arrow.
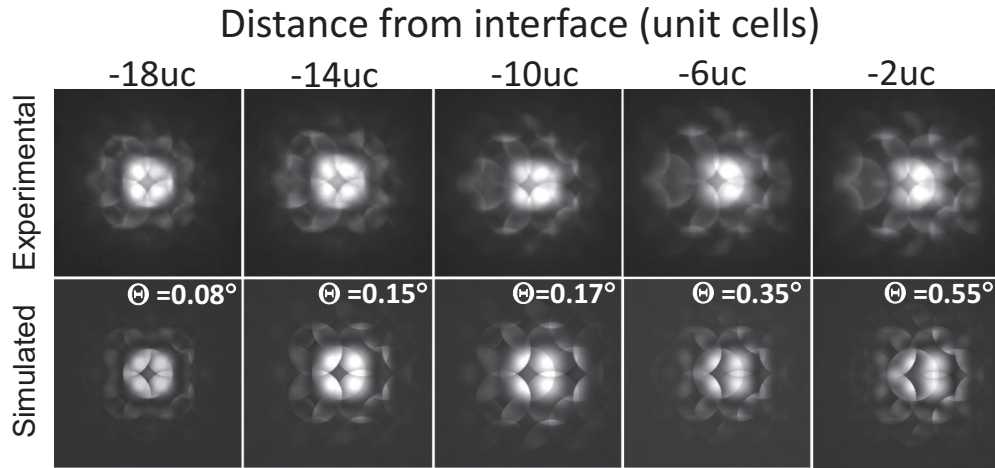
Distance from interface (unit cells)

FIG. 10. Experimental PACBED patterns (top panel) and simulated convergent beam electron diffraction (CBED) patterns (bottom panel) for the [100]-oriented STO/LSMO, as a function of the distance from the STO substrate to the interface at 0 u.c. The acquisition step was 0.35 nm. To improve the signal/noise ratio, the patterns in the figure were averaged by four neighboring patterns. It can be seen that the CBED patterns change from nearly symmetric far away for the interface to clear asymmetric near to interface. The tilt angle near the interface was estimated to be around 0.5°.

where $w1$ and $w2$ are the width at half maximum for the left and right side of the peak, respectively, and x_c is the peak position. The ratio of $w1/w2$ ($w12$ ratio) defines the asymmetric deviation. In Figs. 8(d) and 8(e), the intensity profiles of both Sr and Ti columns were fitted with the single-Gaussian and bi-Gaussian functions, respectively. It is obvious that the bi-Gaussian function agrees much better with the intensity profile than the single-Gaussian function. It is interesting to note that the asymmetry deviation is element-dependent, i.e., the higher the atomic number, the larger the deviation. This is particularly critical to the polarization measurements in perovskite where the *A* and *B* site elements are often very different and enhanced or reduced displacements can be introduced, depending on the curling direction. We realize only when such a possible artifact is taken into account can the measurement of atomic polarization be meaningful. Figure 9 presents an example that improper Gaussian fitting can induce significant measurements errors in polarization, which can be removed by the bi-Gaussian fitting method.

3. Existence of small sample curling in STO/LSMO verified by convergent beam electron diffraction

Here we carried out the STEM position-averaged convergent beam electron diffraction (PACBED) experiment to determine the local curling of the film. Figure 10 shows some of the PACBED patterns from the exact same locations where the STEM-HAADF images [Fig. 2(a) in the manuscript] were taken. A comparison between the experimental data and the simulated patterns shows that the tilt angles in the STO near the interface is less than 1°. The shape of TEM samples under surface strain [51,52] is different from our curling picture, which indicates that no obvious strain occurs at the interface of the LSMO/STO.

Due to the presence of the sample curling in thin areas, instead of single-Gaussian fitting, we used bi-Gaussian fitting to measure the atomic positions in the HAADF-STEM image [Fig. 2(a) in the manuscript]. The curling-induced errors on the displacements can be removed, and the intrinsic polarization can be extracted from the images. We emphasize that, after the curling effect was removed from our measurements, anomalously deep polarization still exists in STO near the interfaced with LSMO.

4. Simulation parameters of HAADF-STEM image and CBED pattern of STO

The STEM images of noncurling and curling STO were simulated based on the multislice method. Phonons are considered in the calculation by adding random displacements to atoms from their lattice sites using the Gaussian function with their corresponding Debye-Waller factors. The slice thickness used in our simulations is 1.95 Å. A probe about 0.8 Å was generated using the following parameters: electric voltage of 200 kV, spherical aberration of 0.0096 mm, and defocus of 12 Å. The HAADF detector was set with 67 and 275 mrad as inner and outer collection angles. The channeling effect of the incident electron beam along atomic columns was also considered in the simulations. Crystal thickness used in our simulations is about 35 nm based on both the CBED and EELS estimations. The changes of sample thickness will affect the amount of asymmetric deviation. However, the quantification of displacements measurements by bi-Gaussian fitting method is much less thickness-dependent, indicated by our image simulation and fitting results. The Bloch wave method was used to simulate the CBED patterns.

---

[1] H. Y. Hwang, Y. Iwasa, M. Kawasaki, B. Keimer, N. Nagaosa, and Y. Tokura, Nat. Mater. **11**, 103 (2012).

[2] J. Jak Chakhalian, J. W. Freeland, A. J. Millis, C. Panagopoulos, and J. M. Rondinelli, Rev. Mod. Phys. **86**, 1189 (2014).

[3] C. H. Ahn, A. Bhattacharya, M. Di Ventra, J. N. Eckstein, C. D. Frisbie, M. E. Gershenson, A. M. Goldman, I. H. Inoue, J. Mannhart, A. J. Millis, A. F. Morpurgo, D. Natelson, and J.-M. Triscone, Rev. Mod. Phys. **78**, 1185 (2006).

[4] M. Bibes, E. V. Javier, and A. Barthélémy, Adv. Phys. **60**, 5 (2010).

[5] S. Okamoto and A. Millis, Nature **428**, 630 (2004).

[6] N. Nakagawa, H. Y. Hwng, and D. A. Muller, Nat. Mater. **5**, 204 (2006).

[7] R. Pentcheva and W. E. Pickett, Phys. Rev. Let. **102**, 107602 (2009).

[8] A. Ohtomo and H. Y. Hwang, Nature **427**, 423 (2004).

[9] N. Reyren, S. Thiel, A. D. Caviglia, L. F. Kourkoutis, G. Hammerl, C. Richter, C. W. Schneider, T. Kopp, A.-S. Rüetschi, D. Jaccard, M. Gabay, D. A. Muller, J.-M. Triscone, and J. Mannhart, Science **317**, 1196 (2007).

[10] J.-F. Ge, Z.-L. Liu, C. Liu, C.-L. Gao, D. Qian, Q.-K. Xue, Y. Liu, and J.-F. Jia, Nature Mater. **14**, 285 (2015).

[11] W. Meevasana, P. D. C. King, R. H. He, S.-K. Mo, M. Hashimoto, A. Tamai, P. Songsiriritthigul, F. Baumberger, and Z-X. Shen, Nature Materials **10**, 114 (2011).

[12] S. M. Walker, F. Y. Bruno, Z. Wang, A. de la Torre, S. Riccó, A. Tamai, T. K. Kim, M. Hoesch, M. Shi, M. S. Bahramy, P. D. C. King, and F. Baumberger, Adv. Materials **27**, 3894 (2015).

[13] P. R. Willmott, S. A. Pauli, R. Herger, C. M. Schlepütz, D. Martoccia, B. D. Patterson, B. Delley, R. Clarke, D. Kumah, C. Cionca, and Y. Yacoby, Phys. Rev. Lett. **99**, 155502 (2007).

[14] A. S. Kalabukhov, Y. A. Boikov, I. T. Serenkov, V. I. Sakharov, V. N. Popok, R. Gunnarsson, J. Börjesson, N. Ljustina, E. Olsson, D. Winkler, and T. Claeson, Phys. Rev. Lett. **103**, 146101 (2009).

[15] W. Siemons, G. Koster, H. Yamamoto, W. A. Harrison, G. Lucovsky, T. H. Geballe, D. H. A. Blank, and M. R. Beasley, Phys. Rev. Lett. **98**, 196802 (2007).

[16] G. Herranz, M. Basletić, M. Bibes, C. Carrétéro, E. Tafra, E. Jacquet, K. Bouzehouane, C. Deranlot, A. Hamzić, J.-M. Broto, A. Barthélémy, and A. Fert, Phys. Rev. Lett. **98**, 216803 (2007).

[17] G. Berner, M. Sing, H. Fujiwara, A. Yasui, Y. Saitoh, A. Yamasaki, Y. Nishitani, A. Sekiyama, N. Pavlenko, T. Kopp, C. Richter, J. Mannhart, S. Suga, and R. Claessen, Phys. Rev. Lett. **110**, 247601 (2013).

[18] L.P. Yu and A. Zunger, Nature Commun. **5**, 5118 (2014).

[19] B. M. Zhang, L. J. Wu, W. G. Yin, C. J. Sun, P. Yang, T. Venkatesan, J. S. Chen, Y. Zhu, and G. M. Chow, Nano Lett. **16**, 4174 (2016).

[20] C. L. Jia, S. B. Mi, M. Faley, U. Poppe, J. Schubert, and K. Urban, Phys. Rev. B **79**, 081405 (2009).

[21] M. Salluzzo, S. Gariglio, X. Torrelles, Z. Ristic, R. Di Capua, J. Drnec, M. Moretti Sala, G. Ghiringhelli, R. Felici, and N. B. Brookes, Adv. Mat. **25**, 2333 (2013).

[22] C. Cantoni, J. Gazquez, F. M. Granozio, M. P. Oxley, M. Varela, A. R. Lupini, S. J. Pennycook, C. Aruta, U. S. Uccio, P. Perna, and D. Maccariello, Adv. Mater. **24**, 3952 (2012).

[23] K. A. Müller and H. Burkard, Phys. Rev. B **19**, 3593 (1979).

[24] S. E. Rowley, L. J. Spalek, R. P. Smith, M. P. M. Dean, M. Itoh, J. F. Scott, G. G. Lonzarich, and S. S. Saxena, Nat. Phys. **10**, 367 (2014).

[25] P. A. Fleury and J. M. Worlock, Phys. Rev. **174**, 613 (1968).

[26] J. G. Bednorz and K. A. Müller, Phys. Rev. Lett. **52**, 2289 (1984).

[27] A. Chen, Z. Yu, J. Scott, A. Loidl, R. Guo, A. S. Bhalla, and L. E. Cross, J. Phys. Chem. Solids **61**, 191 (2000).

[28] M. Itoh, R. Wang, Y. Inaguma, T. Yamaguchi, Y-J. Shan, and T. Nakamura, Phys. Rev. Lett. **82**, 3540 (1999).

[29] J. H. Haeni, P. Irvin, W. Chang, R. Uecker, P. Reiche, Y. L. Li, S. Choudhury, W. Tian, M. E. Hawley, B. Craigo, A. K. Tagantsev, X. Q. Pan, S. K. Streiffer, L. Q. Chen, S. W. Kirchoefer, J. Levy, and D. G. Schlom, Nature **430**, 758 (2004).

[30] Z. Liao, F. Li, P. Gao, L. Li, J. Guo, X. Q. Pan, R. Jin, E. W. Plummer, and Jiandi ZhangPhys. Rev. B **92**, 125123 (2015).

[31] C.-L. Jia, V. Nagarajan, J.-Q. He, L. Houben, T. Zhao, R. Ramesh, K. Urban, and R. Waser, Nature Mater. **6**, 64 (2007).

[32] C.-L. Jia, S.-B. Mi, K. Urban, I. Vrejoiu, M. Alexe, and D. Hesse, Nature Mater. **7**, 57 (2008).

[33] W. Zhong, R. D. King-Smith, and D. Vanderbilt, Phys. Rev. Lett. **72**, 3618 (1994).

[34] H. W. Jang, A. Kumar, S. Denev, M. D. Biegalski, P. Maksymovych, C. W. Bark, C. T. Nelson, C. M. Folkman, S. H. Baek, N. Balke, C. M. Brooks, D. A. Tenne, D. G. Schlom, L. Q. Chen, X. Q. Pan, S. V. Kalinin, V. Gopalan, and C. B. Eom, Phys. Rev. Lett. **104**, 197601 (2010).

[35] D. A. Muller, L. Fitting Kourkoutis, M. Murfitt, J. H. Song, H. Y. Hwang, J. Silcox, N. Dellby, and O. L. Krivanek, Science, **319**, 1073 (2008).

[36] L. Chen, Z. Wang, G. Wang, H. Guo, M. Saghayezhian, J. Tao, Y. Zhu, E.W. Plummer, and Jiandi Zhang (unpublished).

[37] D. A. Muller, N. Nakagawa, A. Ohtomo, J. L. Grazul, and H. Y. Hwang, Nature, **430**, 657 (2004).

[38] M. Varela, M. P. Oxley, W. Luo, J. Tao, M. Watanabe, A. R. Lupini, S. T. Pantelides, and S. J. Pennycook, Phys. Rev. B **79**, 085117 (2009).

[39] A. Hoffmann, S. G. E. te Velthuis, Z. Sefrioui, J. Santamaría, M. R. Fitzsimmons, S. Park, and M. Varela, Phys. Rev. B **72**, 140407 (R) (2005).

[40] F. Pailloux, D. Imhoff, T. Sikora, A. Barthélémy, J.-L. Maurice, J.-P. Contour, C. Colliex, and A. Fert, Phys. Rev. B **66**, 014417 (2002).

[41] M.-G. Han, M. S. J. Marshall, L. Wu, M. A. Schofield, T. Aoki, R. Twesten, J. Hoffman, F. J. Walker, C. H. Ahn, and Y. Zhu, Nat. Commun. **5**, 4693 (2014).

[42] A. S. Barker, Jr. and M. Tinkham, Phys. Rev. **125**, 1527 (1962).

[43] A. F. Devonshire, Philos. Mag. **3**, 85 (1954).

[44] J. P. Perdew, K. Burke and M. Ernzerhof, Phys. Rev. Lett. **77**, 3865 (1996).

[45] P. E. Blochl, Phys. Rev. B **50**, 17953 (1994).

[46] G. Kresse and J. Furthmüller, Comput. Mater. Sci. **6**, 15 (1996).

[47] S. L. Dudarev, G. A. Botton, S. Y. Savrasov, C. J. Humphreys, and A. P. Sutton, Phys. Rev. B **57**, 1505 (1998).

[48] L. Yu, V. Ranjan, W. Lu, J. Bernholc, and M. Buongiorno Nardelli, Phys. Rev. B **77**, 245102 (2008).

[49] M. Nakamura, A. Sawa, J. Fujioka, M. Kawasaki, and Y. Tokura, Phys. Rev. B **82**, 201101 (2010).

[50] A. Sawa, A. Yamamoto, H. Yamada, T. Fujii, M. Kawasaki, J. Matsuno, and Y. Tokura, App. Phys. Lett. **90**, 252102 (2007).

[51] F. Banhart, Ultramicroscopy, **56**, 233 (1994).

[52] F. Houdellier, C. Roucau, L. Clément, J. L. Rouvière, and M. J. Casanove, Ultramicroscopy **106**, 951 (2006).